# Andreev reflection in ballistic normal metal/graphene/superconductor junctions

P. Pandey,[1] R. Kraft,[1] R. Krupke,[1,2] D. Beckmann [1,*] and R. Danneau [1,†]

[1]*Institute of Nanotechnology, Karlsruhe Institute of Technology, D-76021 Karlsruhe, Germany*
[2]*Department of Materials and Earth Sciences, Technical University Darmstadt, D-64287 Darmstadt, Germany*

We report the study of ballistic transport in normal metal/graphene/superconductor junctions in edge-contact geometry. While in the normal state, we have observed Fabry-Pérot resonances suggesting that charge carriers travel ballistically, the superconducting state shows that the Andreev reflection at the graphene/superconductor interface is affected by these interferences. Our experimental results in the superconducting state have been analyzed and explained with a modified Octavio-Tinkham-Blonder-Klapwijk model taking into account the magnetic pair-breaking effects and the two different interface transparencies, i.e., between the normal metal and graphene, and between graphene and the superconductor. We show that the transparency of the normal metal/graphene interface strongly varies with doping at large scale, while it undergoes weaker changes at the graphene/superconductor interface. When a cavity is formed by the charge transfer occurring in the vicinity of the contacts, we see that the transmission probabilities follow the normal state conductance highlighting the interplay between the Andreev processes and the electronic interferometer.

## I. INTRODUCTION

In his seminal work, Andreev calculated that an electron has a finite probability to be retroreflected as a hole at the interface between a normal metal (N) and a superconductor (S) [1]. This phenomenon known as Andreev reflection has been extensively studied in normal metal-superconductor junctions [2–5] and strongly depends on the quality of the NS interface [6–9]. NS junctions have been used to realize Cooper-pair splitters indicating their significance in quantum entanglement [10–16]. Owing to its electronic band structure and its tunability, graphene in contact with a superconducting material exhibits gate controlled unusual conductance [17] and Andreev processes with rich subharmonic gap structures [18] and specular reflection at very low energy [19–24], i.e., near the charge neutrality point. This exotic effect could potentially be used to detect valley polarization [25] or in spin filters [26], while Andreev conversion effects may persist in the quantum Hall regime [27–30]. Noticeably, an NS interface coupled to a one-dimensional system with strong spin-orbit coupling is expected to host Majorana bound states [31].

The development of van der Waals heterostructures designed from two-dimensional materials [32–34] in addition to the recent progresses in sample fabrication [35,36], dramatically improved both charge carrier mobility and contact transparency in graphene-based electrical devices. As a consequence, the study of proximity induced superconductivity regained interest with the possibilities to measure large supercurrents and ballistic interferences [37–50]. However, most of the studies related to Andreev processes in this system usually consist of probing the dissipationless current

and multiple Andreev reflection in graphene connected to two superconducting contacts, while Andreev bound states in graphene have been detected by tunneling spectroscopy experiments [51]. Indeed, very few utilize devices with a single superconducting-graphene interface [23,52,53] that can be described by the Blonder-Tinkham-Klapwijk (BTK) model [6]. To our knowledge, there is no experimental study on normal metal-graphene-superconductor (NGS) junctions in the ballistic regime.

Here we investigate NGS devices based on graphene-hexagonal boron nitride (hBN) van der Waals heterostructures. We observe that while the normal state conductance exhibits Fabry-Pérot (FP)-like interference, the electronic transport and the Andreev processes at the GS interface in the superconducting state are very well described by our modified Octavio-Tinkham-Blonder-Klapwijk (OTBK) model [6,7,54,55]. We show that the transmission probabilities extracted from the experimental data follow the same oscillating trend as the normal state conductance which reflects the ballistic nature of the electronic transport in these clean systems.

## II. SAMPLE DESIGN, FABRICATION PROCESS, AND EXPERIMENTAL DETAILS

We have fabricated our van der Waals heterostructure using a dry transfer method following a similar technique as described in Wang *et al.* [36]. Graphene and hBN crystallites (16 and 20 nm thick for the top and bottom hBN layer, respectively) were obtained by exfoliation of natural graphite (from NGS Naturgraphit GmbH) and commercial hBN powder (Momentive, grade PT110), respectively, and transferred onto Si substrates with a 300 nm thick $SiO_2$ top layer. Edge contacts to the graphene sheet were established in a self-aligned manner by etching the desired connection area followed by

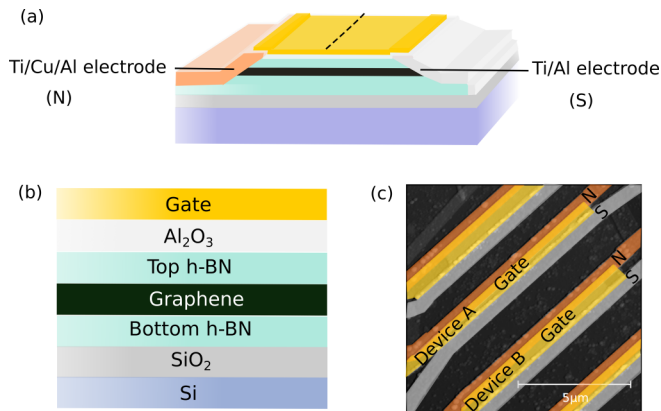*detlef.beckmann@kit.edu
†romain.danneau@kit.edu

FIG. 1. (a) Schematic of the device geometry. (b) Cross section schematic of the studied devices across the dashed line in (a). (c) False color atomic force micrograph of the two devices with normal (N) and superconducting (S) contacts. Scale bar is 5 $\mu$m.



FIG. 2. Resistance $R$ and conductance $G$ versus charge carrier density ($n$) and gate voltage ($V_g$).

metallization as described by Kraft *et al.* [46]. However, this process had to be adapted in order to deposit two different metals. The contact geometry is defined by standard e-beam lithography where polymethyl methacrylate (PMMA) was used as a mask, followed by reactive ion etching (RIE) with a plasma of CHF$_3$ and O$_2$ through the van der Waals heterostructure to define the first edge contact to the graphene sheet. Immediately after RIE, the first electrode metal is evaporated under ultrahigh vacuum (pressure of the order of $10^{-9}$ mbar). This procedure is repeated as two different metals have to be deposited for the contact electrodes. We used Ti/Al (5 and 70 nm, respectively) for the superconducting electrode and Ti/Cu/Al (5, 70, and 5 nm, respectively) for the normal metal electrode. The Al and Cu contacts are parallel. While Ti serves as an adhesive layer, the 5 nm Al in the normal electrode serves as a capping layer to protect Cu from oxidation. In the final fabrication step, a 25 nm thick Al$_2$O$_3$ layer was deposited on top of these devices by atomic layer deposition, followed by the fabrication of a top gate made of Ti/Cu/Al (5, 80, and 5 nm, respectively).

Schematics of the devices are shown in Figs. 1(a) and 1(b) and an AFM micrograph of the measured devices (A and B) is shown in Fig. 1(c). These devices have high width over length $W/L$ ratio with dimensions of $W = 6$ $\mu$m, $L = 0.25$ $\mu$m and $W = 5$ $\mu$m, $L = 0.45$ $\mu$m, respectively. The data presented in the main text is from device A unless stated otherwise. Similar data was obtained from device B except the FP resonances which were observed only in device A. Electrical characterization of these devices was carried out in a $^3$He/$^4$He dilution refrigerator at a base temperature $T$ in the range of 20–100 mK unless otherwise mentioned. All of the measurements were conducted in a pseudo-four-probe configuration with standard low frequency lock-in detection technique.

### III. BALLISTIC TRANSPORT WITH ASYMMETRICAL CONTACT IN THE NORMAL STATE

In this section we show how the asymmetry of the contacts tunes the FP resonances characterizing the ballistic regime
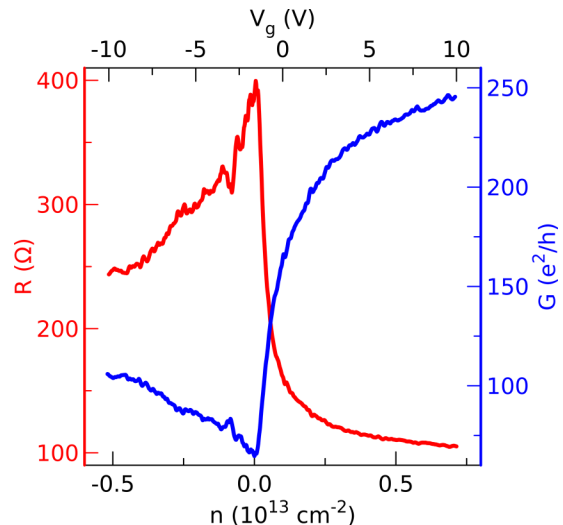
of our two-terminal devices in the normal state. Figure 2 displays both resistance $R$ and conductance $G$ of device A as a function of gate voltage $V_g$ and charge carrier density $n$ at $T \sim 4.2$ K. The charge carrier density $n$ was obtained from Shubnikov–de Haas measurements as a function of gate voltage $V_g$. We observe asymmetry in the curves, i.e., higher resistance in the hole-doped ($p$) region than the electron-doped ($n$) region, and shift of the charge neutrality point (CNP) towards negative gate voltage. It indicates $n$-type doping of the graphene sheet and formation of a potential barrier at the contact while driving the Fermi level in the valence band [56–58]. We note that as the two contacts are made of different materials (Ti/Cu/Al and Ti/Al), the charge transfer induced by the different work function of the leads might enhance this asymmetry. Since the graphene sheet is $n$-type doped by the metal contacts, driving the charge transport in graphene to hole-doped regime using the gate results in the formation of $pn$ junctions in the vicinity of the metal electrodes. These two $pn$ junctions act as partially transmitting interfaces similar to the mirrors in a FP interferometer. As a result, charge carriers are reflected back and forth at the graphene/metal interfaces. Quantum interference takes place due to multiply reflected charge carrier trajectories. Varying the gate voltage changes the Fermi wavelength which leads to an alternating constructive and destructive interference pattern in conductance. For a ballistic device, it can be observed as a periodic oscillation of conductance/resistance while tuning the Fermi wavelength. These oscillations can be clearly seen in the $p$-doped region in Fig. 2 and can be attributed to FP interference as a cavity is formed while the Fermi level is positioned in the valence band [59–67].

In the simplest case, for devices with high aspect ratio, FP resonances occur when the condition $k_F L_C = n\pi$ is satisfied, where $k_F$ is the Fermi wave vector, $L_C$ is the cavity length, and $n$ is an integer. Considering normal incidence of charge carriers at a fixed bias, $L_C$ can be estimated by the change in the Fermi wave vector/wavelength between two consecutive conductance maxima/minima. We have used both bias
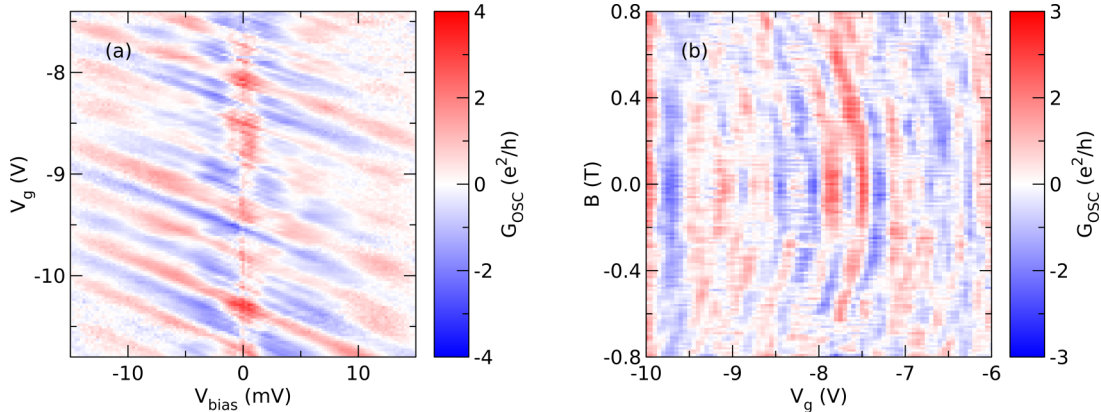
FIG. 3. Energy dependence and magnetic field dispersion of the FP interference in the hole-doped region: (a) $G_{osc}$ versus applied bias voltage $V_{bias}$ and gate voltage $V_g$ showing asymmetric pattern of the FP resonances at temperature $T = 100$ mK and magnetic field $B = 50$ mT. (b) $G_{osc}$ versus magnetic field $B$ and gate voltage $V_g$.

spectroscopy and magnetic field dependence to characterize the FP interference. As the conductance profile strongly varies when the gate voltage $V_g$, bias voltage $V_{bias}$, or magnetic field $B$ are tuned [62,67], we have extracted the oscillatory part of the conductance $G_{osc}$ by subtracting a nonoscillatory background contribution in order to study this interference effect. Figure 3(a) shows the bias spectroscopy map of $G_{osc}$ versus gate and bias voltages $V_g$ and $V_{bias}$, respectively. We note that the usual checkerboard pattern observed in bias spectroscopy experiments [60,63,64] is very asymmetric here as it was observed in carbon nanotubes with energy-dependent transmission coefficients implying strong asymmetry between the leads [68]. Here the two different materials used to contact the graphene can possibly explain our bias spectroscopy pattern as the two interfaces most likely have different transparencies. We note that the asymmetry of the contacts might affect the visibility of these quantum oscillations. The interference pattern observed here corresponds to a cavity length $L_C$ of $240 \pm 5$ nm which is consistent with the geometrical dimension of the device, confirming that the cavity is formed by the *pn* junctions arising from the charge transfer in the vicinity of the contacts [56–58].

Thanks to the angle dependence of the transmission through a potential barrier in graphene, an effect known as Klein tunneling [59], FP interference can also be tuned and studied by applying a perpendicular magnetic field $B$. Figure 3(b) displays the effect of low magnetic field on the FP interference pattern before entering the quantum Hall regime, where a parabolic dispersion of the interference can be observed due to the Aharonov-Bohm phase. As already observed in FP interferometers [62,64,65], when $B$ increases, the charge carrier trajectories within the cavity bend up to the point that, in the momentum space, the path encloses the origin picking up a nontrivial Berry phase of $\pi$ [62]. Experimentally, this appears as a phase shift of $\pi$ in the conductance/resistance oscillations [62,64,65] at a certain magnetic field as seen in Fig. 3(b). It is to be noted that this measurement was carried out in another cool down which accounts for the slight change in the position of conductance maxima/minima as compared to Fig. 3(a) with respect to the applied gate voltage.

## IV. ANDREEV REFLECTION AND INTERFACE ANALYSIS IN NGS JUNCTIONS

In the previous section we have seen that the FP interference in the normal state is affected by the asymmetry of the leads. Here we investigate the superconducting state and observe that the ballistic nature of the quasiparticle transport is also visible at the graphene/superconductor interface. In order to study superconductivity in these NGS junctions, we measured series of differential conductance $dI/dV$ spectra as a function of gate voltage $V_g$, perpendicular magnetic field $B$, and temperature $T$, and compare our data with a modified OTBK model [7] combined with Ref. [54] (without accounting for different spin density of states). We then analyze the resulting fitting parameters and observe that the interface transparencies follow the oscillatory behavior of the conductance due to FP interference as an asymmetrical cavity is built in our devices.

### A. Modeling

To account for the two separate interfaces of our NGS structure, we model the system in the superconducting state using a modified OTBK model [7]. The OTBK model was initially developed to describe multiple Andreev reflections in a ballistic SNS junction, and describes the system in terms of a single-channel ideal conductor connected to two superconducting reservoirs by identical junctions. We modify the model to account for our devices as follows: First, the transmission probabilities of the two interfaces can be different, and second, one of the terminals is normal rather than superconducting (which implies that there are no multiple Andreev reflections).

As depicted in Fig. 4, the graphene sheet (G) is modeled as an ideal conductor, connecting a superconducting (S) terminal (right) and a normal metal (N) terminal (left). The interfaces have normal-state transmission probabilities $\tau_S$ and $\tau_N$, respectively. These transmission probabilities summarily account for the material interfaces and the *pn* junctions formed in the *p*-doped region. The superconducting terminal is at electrochemical potential 0, and the normal metal terminal is at electrochemical potential $\mu = -eV$. To calculate the
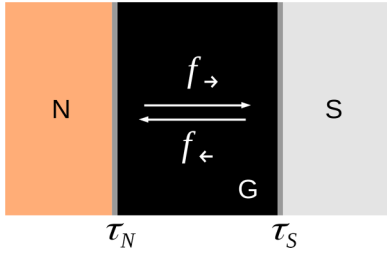
FIG. 4. Schematic view of the model for an NGS junction (see text).

TABLE I. The pair potential $\Delta$, transmission probabilities $\tau_N$ and $\tau_S$, and the effective electronic temperature $T$ as obtained from the fit of the Andreev spectrum shown in Fig. 5(a).

| $V_g$ (V) | $\Delta$ ($\mu$eV) | $\tau_N$ | $\tau_S$ | $T$ (mK) |
|---|---|---|---|---|
| 9.8 | 127 | 0.92 | 0.7 | 354 |
| −9.8 | 144 | 0.73 | 0.69 | 270 |
| −2 | 140 | 0.59 | 0.67 | 190 |

current through the device, we determine the left- and right-moving distribution functions $f_\leftarrow(\epsilon)$ and $f_\rightarrow(\epsilon)$ in the ideal conductor from boundary conditions. At the superconducting terminal, we have [7]

$$f_\leftarrow(\epsilon) = T(\epsilon)f_0(\epsilon) + R(\epsilon)f_\rightarrow(\epsilon) + A(\epsilon)[1 - f_\rightarrow(-\epsilon)],$$
$$f_\rightarrow(\epsilon) = \tau_N f_0(\epsilon - \mu) + r_N f_\leftarrow(\epsilon), \tag{1}$$

where $T(\epsilon)$, $R(\epsilon)$, and $A(\epsilon)$ are the probabilities for normal transmission, normal reflection, and Andreev reflection, respectively, at the superconducting terminal, $r_N = 1 - \tau_N$ is the reflection probability at the normal terminal, $f_0$ is the Fermi function, and $\epsilon$ is the energy.

Equation (1) can be solved analytically, and the current through the device can then be calculated by integrating the difference $f_\rightarrow(\epsilon) - f_\leftarrow(\epsilon)$ over energy. From the current, the differential conductance

$$\frac{dI}{dV} = G_N \int g(\epsilon)\left(-\frac{\partial f_0(\epsilon + eV)}{\partial eV}\right)d\epsilon \tag{2}$$

is obtained. Here $G_N$ is the normal-state conductance, and $g(\epsilon)$ is the normalized spectral conductance in the superconducting state. It is given by

$$g(\epsilon) = \frac{1}{\tau^*}\frac{\tau_N\{A^2(\epsilon)r_N - [R(\epsilon) - 1][R(\epsilon)r_N - 1] - A(\epsilon)\tau_N\}}{\{A^2(\epsilon)r_N^2 - [R(\epsilon)r_N - 1]^2\}},$$

where $\tau^* = \tau_S\tau_N/(1 - r_S r_N)$ is the effective transmission probability in the normal state.

In the original OTBK model, $T(\epsilon)$, $R(\epsilon)$, and $A(\epsilon)$ are calculated using the BTK model [6], which accounts for a ballistic junction of arbitrary transmission probability between a simple BCS [69] superconductor and a normal metal. In contrast, we use a generalized BTK model [54,55], which allows us to incorporate the effect of pair breaking in an applied magnetic field [70] on the spectral properties of the superconducting terminal. In this model, the Andreev and normal reflection probabilities are given by

$$A(\epsilon) = \tau_S^2\left|\frac{\hat{f}(\epsilon)}{D(\epsilon)}\right|^2, \tag{3}$$

$$R(\epsilon) = \frac{4r_S}{|D(\epsilon)|^2}, \tag{4}$$

where $D(\epsilon) = (1 + r_S) + (1 - r_S)\hat{g}(\epsilon)$, and $\hat{g}(\epsilon)$ and $\hat{f}(\epsilon)$ are the normal and anomalous Green's functions of the superconductor, respectively. The latter are subject to the normalization $\hat{g}^2(\epsilon) + \hat{f}^2(\epsilon) = 1$ and have to be determined from the Usadel

equation, which in our case reads [54]

$$\epsilon\hat{f}(\epsilon) + i\alpha\hat{g}(\epsilon)\hat{f}(\epsilon) - i\Delta\hat{g}(\epsilon) = 0, \tag{5}$$

where $\alpha$ is the magnetic depairing energy, and $\Delta$ is the pair potential. Fits of the conductance spectra in an applied field serve as an additional test of the applicability of the model (see experimental section below). Without depairing ($\alpha = 0$), $A(\epsilon)$ and $R(\epsilon)$ reduce to the analytical BTK expressions [6].

To summarize, the parameters entering into the conductance spectrum Eq. (2) are the normal-state conductance $G_N$, the pair potential $\Delta$, the magnetic depairing energy $\alpha$, the transmission probabilities $\tau_S$ and $\tau_N$, and the effective electronic temperature $T$ (via the Fermi function $f_0$).

**B. Experimental results**

Figure 5(a) shows differential conductance $dI/dV$ curves measured as a function of applied bias voltage $V_{bias}$ at zero magnetic field and $T \sim 20$ mK under three different gate conditions, i.e., at $V_g = 9.8$, $-9.8$, and $-2$ V corresponding to the Fermi level sitting in the conduction band, the valence band, and close to the charge neutrality point, respectively. In the subgap regime, we observe Andreev reflections giving rise to nonzero conductance. Contrary to the previous reports on NGS junctions, we do not observe any zero-bias anomaly [52,53] which is usually interpreted as the effect of reflectionless tunneling at the superconductor interface [71–74]. By using the modified OTBK model to fit the data, we obtain variation of $\Delta$ from $\sim$127 $\mu$eV in the $n$-doped region to $\sim$144 $\mu$eV in the $p$-doped region. The fitting parameters used for these $dI/dV$ curves are shown in Table I. The observed difference in $\Delta$ can be seen as the shift in the $dI/dV$ maxima in Fig. 5(a) and it can be attributed to two effects. First, the effective temperature of the device is higher on the electron side due to higher normal state conductance as can be seen in Fig. 2. It can cause self-heating of the device leading to a decrease in $\Delta$. Second, there could be a gate dependent voltage division taking place between the normal metal lead and the graphene sheet.

In order to test the applicability of our model with respect to an applied magnetic field, we have studied the differential conductance $dI/dV$ as a function of perpendicular magnetic field $B$. Figure 5(b) shows a series of $dI/dV$ curves at various $B$ at $V_g = -9.2$ V and a base temperature of $T \sim 20$ mK. While the applied magnetic field is kept below the critical magnetic field $B_C$, thereby preserving superconductivity in the device, a clear decrease in $\Delta$ can be seen in the successive conductance curves. We observe a decrease in $\Delta$ from $\sim$143 $\mu$eV
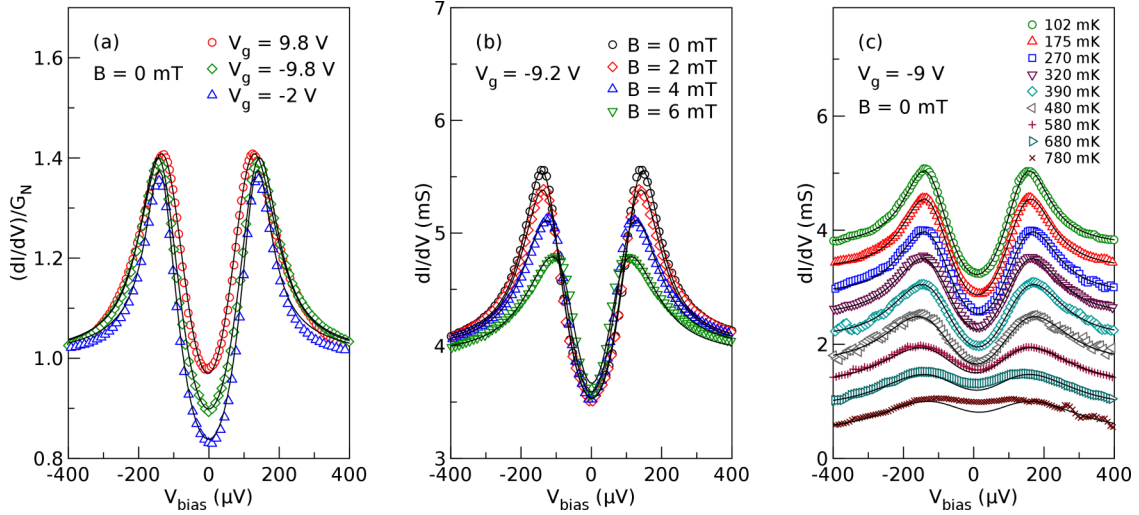
FIG. 5. Differential conductance $dI/dV$ measured as a function of the applied bias voltage $V_{bias}$ for: (a) normalized by the normal state conductance $G_N$ (from the measurement at 4.2 K) for applied gate voltage $V_g$ at $T \sim 20$ mK corresponding to electron-doped region (circle), hole-doped region (diamond), and close to the charge neutrality point (triangle). (b) Under various values of perpendicular magnetic field $B$ at $T \sim 20$ mK and $V_g = -9.2$ V corresponding to the hole-doped region. (c) For different temperatures at $V_g = -9$ V, i.e., in the the hole-doped region. In all panels, the symbols represent experimental data and the solid curves represent the best fit of the data with our model.

at 0 mT down to $\sim$125 $\mu$eV at 6 mT while the magnetic depairing energy $\alpha$, accounting for magnetic pair-breaking effects [70,75], changes from 0 to $\sim$0.18$\Delta$. Table II shows the change in $\Delta$ and $\alpha$ as extracted from the fits of the data.

Superconductivity weakens as the temperature starts to rise to the critical temperature $T_C$. In order to see the evolution of superconductivity in our devices, we measured a series of temperature dependent conductance spectra ranging from $T \sim 102$ to 780 mK in the hole-doped regime at $V_g = -9$ V under zero magnetic field. It can be clearly seen in Fig. 5(c) that $\Delta$ decreases with increasing temperature and the system goes towards the normal state. For the sake of clarity, the differential conductance curves have been shifted downward by 0.4 mS in successive steps. The series can be well captured with the fits obtained from the modified OTBK model. With increasing temperature, $\Delta$ decreases from $\sim$144 to $\sim$119 $\mu$eV. As can be seen, in the low temperature regime, the model provides reasonable fit of the data. However, as the temperature approaches $T_C$, the data is not very well fitted by the model. It shows the limitation of the model close to $T_C$.

Table III summarizes the transmission probabilities $\tau_N$ and $\tau_S$ of the normal metal/graphene and

graphene/superconductor interface, respectively, including the error bars as extracted from the fits shown in Figs. 5(a), 5(b), and 5(c). In our devices, the two different interfaces, namely the normal metal/graphene and the graphene/superconductor interfaces, play a crucial role in the electronic transport. Figure 6(a) displays $\tau_N$ and $\tau_S$ over a large gate voltage range for device B and in a selected gate voltage range for device A. Both transparencies are extracted from our $dI/dV$ fits. In case of device A, the transmission probability for the normal metal/graphene interface $\tau_N$ obtained from the fits varies from 0.74 in the $p$-doped region to 0.92 in the $n$-doped region, dropping to 0.59 close to the charge neutrality point. The transmission probability for the graphene/superconductor interface $\tau_S$, on the other hand, varies from 0.67 to 0.71 for the entire gate voltage range indicating a weak barrier at the interface. In case of device B, we have obtained lower transmission probability for the normal metal/graphene interface as compared to device A, however, the dependence of $\tau_N$ and $\tau_S$ on the applied gate voltage follows the same trend as device A. Note that this systematic dependence of the transmission probabilities on doping is directly visible in the change of the normalized

TABLE II. The pair potential $\Delta$ and the magnetic depairing energy $\alpha$ as obtained from the fit of the Andreev spectrum shown in Fig. 5(b). The effective electronic temperature $T$ was 265 mK and the transmission probabilities $\tau_N$ and $\tau_S$ were 0.73 and 0.69, respectively, for all of the fits.

| $B$ (mT) | $\Delta$ ($\mu$eV) | $\alpha$ ($\Delta$) |
|---|---|---|
| 0 | 143 | 0 |
| 2 | 143 | 0.03 |
| 4 | 136 | 0.09 |
| 6 | 125 | 0.18 |

TABLE III. Transmission probabilities $\tau_N$ and $\tau_S$ including the error bars as extracted from the fits shown in Figs. 5(a), 5(b), and 5(c).

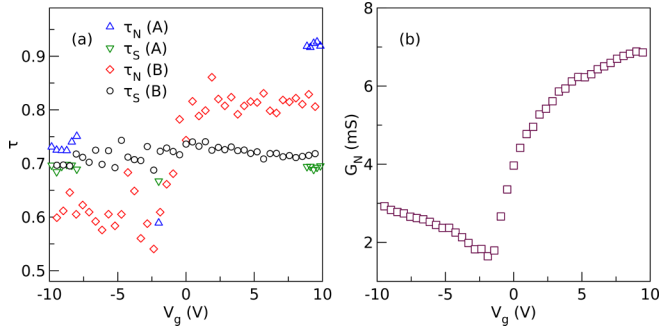| Fig. 5 | $V_g$ (V) | $\tau_N$ | $\tau_S$ |
|---|---|---|---|
| (a) | 9.8 | $0.922 \pm 0.01$ | $0.697 \pm 0.002$ |
| (a) | $-9.8$ | $0.729 \pm 0.008$ | $0.694 \pm 0.003$ |
| (a) | $-2$ | $0.589 \pm 0.006$ | $0.667 \pm 0.002$ |
| (b) | $-9.2$ | $0.73 \pm 0.017$ | $0.692 \pm 0.004$ |
| (c) | $-9$ | $0.743 \pm 0.023$ | $0.675 \pm 0.006$ |

FIG. 6. (a) Transmission probabilities $\tau_N$ and $\tau_S$ of the normal metal/graphene and graphene/superconducting interface, respectively for device A and B. (b) Normal state conductance $G_N$ as a function of gate voltage $V_g$ covering a large scale of charge carrier density in device B. All the $\tau_N$, $\tau_S$, and $G_N$ are obtained from the best fitting values of differential conductance data measured at a base temperature of 20 mK and $B = 0$ T using our modified OTBK model.

subgap conductance in Fig. 5(a). The difference between $\tau_N$ and $\tau_S$ extracted with our model confirms the asymmetry of the interference patterns observed in the differential conductance map in the normal state presented in Fig. 3(a). Figure 6(b) shows the extracted normal state conductance $G_N$ for device B as a function of gate voltage $V_g$ where a large difference between hole and electron conductance is observed due to the $n$ doping of the contact as mentioned before.

For a more detailed analysis of the correlation between the gate dependent normal state conductance and transmission probabilities, we measured a series of conductance spectra at $B = 0$ T with varying $V_g$ in the $p$-doped region at high charge carrier densities for device A. Figure 7(a) shows the normal conductance $G_N$ as circular data points obtained from these measurements as a function of $V_g$. The values of $G_N$ obtained as a fitting parameter from the OTBK fits of the experimental data are plotted as diamonds in Fig. 7(a) showing oscillations similar to the FP interference observed in Fig. 2. In Fig. 7(b), the transmission probabilities obtained from the same fits are shown. It is clear that our fits can qualitatively describe the observed conductance oscillations in terms of transmission probability. It suggests that the transmittance of the interfaces is tuned by $V_g$ in a similar manner as observed for the FP interference. The oscillation period observed here also corresponds to a cavity length $L_C$ of $\sim 236 \pm 10$ nm. It proves that these oscillations indeed arise from the FP interference of the Andreev reflected charge carriers. In a Josephson junction, existence of FP interference can be observed in the superconducting state by following the oscillations in the critical current [37–50] or multiple Andreev reflection [42]. However, to the best of our knowledge, it is the first time that the effect of FP resonances have been observed in superconducting state in NGS junctions.
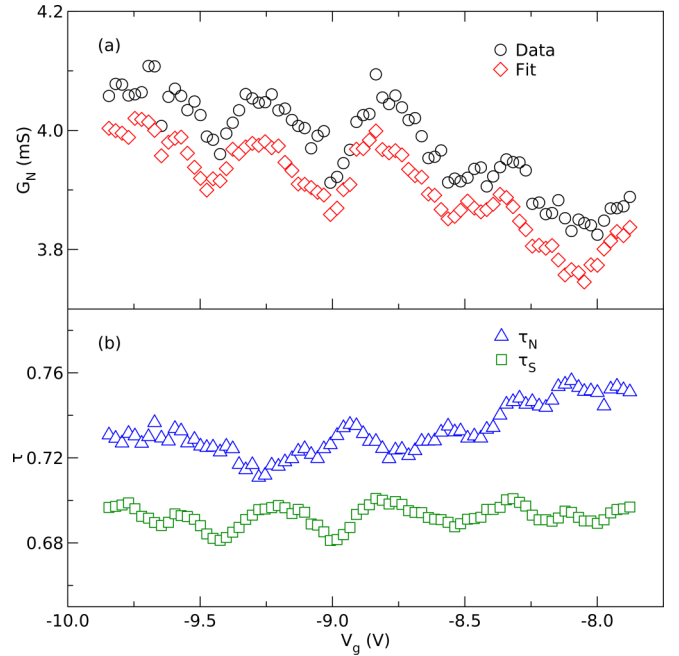


FIG. 7. (a) Oscillations in the normal conductance $G_N$ observed at a base temperature of 20 mK and $B = 0$ T as a function of gate voltage $V_g$ in the hole-doped region (circles), and best fitting value for the conductance obtained from the OTBK fits of the experimental data (diamonds). (b) Transmission probability $\tau$ obtained from the OTBK fits of the experimental data.

## V. CONCLUSION

To conclude, we have reported a study of normal metal/graphene/superconductor junctions in the ballistic regime. We see that in the normal state, the differential conductance shows asymmetric Fabry-Pérot interference when a cavity is formed by charge transfer at the contacts. We have attributed the asymmetry to the different transmissions of the two metal/graphene contact interfaces in our devices. In the superconducting state, the junctions are well described by our modified OTBK model. The Fabry-Pérot interference of the electronic transport is directly reflected in the transmission probabilities in these systems.

[1] A. F. Andreev, The thermal conductivity of the intermediate state in superconductors, Sov. Phys. JETP **19**, 1228 (1964).

[2] C. W. J. Beenakker, Random-matrix theory of quantum transport, Rev. Mod. Phys. **69**, 731 (1997).

[3] H. Courtois, P. Charlat, Ph. Gandit, D. Mailly, and B. Pannetier, The spectral conductance of a proximity superconductor and the reentrance effect, J. Low Temp. Phys. **116**, 187 (1999).

[4] M. Tinkham, *Introduction to Superconductivity* (Courier Dover, New York, 2012).

[5] T. M. Klapwijk, Proximity effect from an Andreev perspective, J. Supercond. **17**, 593 (2004).

[6] G. E. Blonder, M. Tinkham, and T. M. Klapwijk, Transition from metallic to tunneling regimes in superconducting microconstrictions: Excess current, charge imbalance, and supercurrent conversion, Phys. Rev. B **25**, 4515 (1982).

[7] M. Octavio, M. Tinkham, G. E. Blonder, and T. M. Klapwijk, Subharmonic energy-gap structure in superconducting constrictions, Phys. Rev. B **27**, 6739 (1983).

[8] A. Tselev, Y. Yang, J. Zhang, P. Barbara, and S. E. Shafranjuk, Carbon nanotubes as nanoscale probes of the superconducting proximity effect in Pd-Nb junctions, Phys. Rev. B **80**, 054504 (2009).

[9] I. P. Nevirkovets, S. E. Shafranjuk, O. Chernyashevskyy, N. Masilamani, and J. B. Ketterson, Current-voltage characteristics of Nb-carbon-Nb junctions, Low Temp. Phys. **40**, 191 (2014).

[10] L. Hofstetter, S. Csonka, J. Nygård, and C. Schönenberger, Cooper pair splitter realized in a two-quantum-dot Y-junction, Nature (London) **461**, 960 (2009).

[11] L. G. Herrmann, F. Portier, P. Roche, A. L. Yeyati, T. Kontos, and C. Strunk, Carbon Nanotubes as Cooper-Pair Beam Splitters, Phys. Rev. Lett. **104**, 026801 (2010).

[12] L. Hofstetter, S. Csonka, A. Baumgartner, G. Fülöp, S. d'Hollosy, J. Nygård, and C. Schönenberger, Finite-Bias Cooper Pair Splitting, Phys. Rev. Lett. **107**, 136801 (2011).

[13] J. Schindele, A. Baumgartner, and C. Schönenberger, Near-Unity Cooper Pair Splitting Efficiency, Phys. Rev. Lett. **109**, 157002 (2012).

[14] J. Schindele, A. Baumgartner, R. Maurand, M. Weiss, and C. Schönenberger, Nonlocal spectroscopy of Andreev bound states, Phys. Rev. B **89**, 045422 (2014).

[15] Z. B. Tan, D. Cox, T. Nieminen, P. Lähteenmäki, D. Golubev, G. B. Lesovik, and P. J. Hakonen, Cooper Pair Splitting by Means of Graphene Quantum Dots, Phys. Rev. Lett. **114**, 096602 (2015).

[16] I. V. Borzenets, Y. Shimazaki, G. F. Jones, M. F. Craciun, S. Russo, M. Yamamoto, and S. Tarucha, High efficiency CVD graphene-lead (Pb) Cooper pair splitter, Sci. Rep. **6**, 23051 (2016).

[17] A. R. Akhmerov and C. W. J. Beenakker, Pseudodiffusive conduction at the Dirac point of a normal-superconductor junction in graphene, Phys. Rev. B **75**, 045426 (2007).

[18] J. C. Cuevas and A. Levy Yeyati, Subharmonic gap structure in short ballistic graphene junctions, Phys. Rev. B **74**, 180501(R) (2006).

[19] C. W. J. Beenakker, Specular Andreev Reflection in Graphene, Phys. Rev. Lett. **97**, 067007 (2006).

[20] M. Titov, A. Ossipov, and C. W. J. Beenakker, Excitation gap of a graphene channel with superconducting boundaries, Phys. Rev. B **75**, 045417 (2007).

[21] C. W. J. Beenakker, Andreev reflection and Klein tunneling in graphene, Rev. Mod. Phys. **80**, 1337 (2008).

[22] K. Komatsu, C. Li, S. Autier-Laurent, H. Bouchiat, and S. Guéron, Superconducting proximity effect in long superconductor/graphene/superconductor junctions: From specular Andreev reflection at zero field to the quantum Hall regime, Phys. Rev. B **86**, 115412 (2012).

[23] D. K. Efetov, L. Wang, C. Handschin, K. B. Efetov, J. Shuang, R. Cava, T. Taniguchi, K. Watanabe, J. Hone, C. R. Dean, and P. Kim, Specular interband Andreev reflections at van der Waals interfaces between graphene and NbSe$_2$, Nat. Phys. **12**, 328 (2016).

[24] D. K. Efetov and K. B. Efetov, Crossover from retro to specular Andreev reflections in bilayer graphene, Phys. Rev. B **94**, 075403 (2016).

[25] A. R. Akhmerov and C. W. J. Beenakker, Detection of Valley Polarization in Graphene by a Superconducting Contact, Phys. Rev. Lett. **98**, 157003 (2007).

[26] D. Greenbaum, S. Das, G. Schwiete, and P. G. Silvestrov, Pure spin current in graphene normal-superconductor structures, Phys. Rev. B **75**, 195437 (2007).

[27] D. J. Clarke, J. Alicea, and K. Shtengel, Exotic circuit elements from zero-modes in hybrid superconductor-quantum-Hall systems, Nat. Phys. **10**, 877 (2014).

[28] Z. Hou, Y. Xing, A.-M. Guo, and Q.-F. Sun, Crossed Andreev effects in two-dimensional quantum Hall systems, Phys. Rev. B **94**, 064516 (2016).

[29] G.-H. Lee, K.-F. Huang, D. K. Efetov, D. S. Wei, S. Hart, T. Taniguchi, K. Watanabe, A. Yacoby, and P. Kim, Inducing superconducting correlation in quantum Hall edge states, Nat. Phys. **13**, 693 (2017).

[30] S.-B. Zhang and B. Trauzettel, Perfect Crossed Andreev Reflection in Dirac Hybrid Junctions in the Quantum Hall Regime, Phys. Rev. Lett. **122**, 257701 (2019).

[31] A. Yu. Kitaev, Unpaired Majorana fermions in quantum wires, Phys.-Usp. **44**, 131 (2001).

[32] A. K. Geim and I. V. Grigorieva, Van der Waals heterostructures, Nature (London) **499**, 419 (2013).

[33] K. S. Novoselov, A. Mishchenko, A. Carvalho, and A. H. Castro Neto, 2D materials and van der Waals heterostructures, Science **353**, 461 (2016).

[34] M. Yankowitz, Q. Ma, P. Jarillo-Herrero, and B. J. LeRoy, van der Waals heterostructures combining graphene and hexagonal boron nitride, Nat. Rev. Phys. **1**, 112 (2019).

[35] C. R. Dean, A. F. Young, I. Meric, C. Lee, L. Wang, S. Sorgenfrei, K. Watanabe, T. Taniguchi, P. Kim, K. L. Shepard, and J. Hone, Boron nitride substrates for high-quality graphene electronics, Nat. Nanotechnol. **5**, 722 (2010).

[36] L. Wang, I. Meric, P. Y. Huang, Q. Gao, Y. Gao, H. Tran, T. Taniguchi, K. Watanabe, L. M. Campos, D. A. Muller, J. Guo, P. Kim, J. Hone, K. L. Shepard, and C. R. Dean, One-dimensional electrical contact to a two-dimensional material, Science **342**, 614 (2013).

[37] V. E. Calado, S. Goswami, G. Nanda, M. Diez, A. R. Akhmerov, K. Watanabe, T. Taniguchi, T. M. Klapwijk, and L. M. K. Vandersypen, Ballistic Josephson junctions in edge-contacted graphene, Nat. Nanotech. **10**, 761 (2015).

[38] M. Ben Shalom, M. J. Zhu, V. I. Fal'ko, A. Mishchenko, A. V. Kretinin, K. S. Novoselov, C. R. Woods, K. Watanabe, T. Taniguchi, A. K. Geim, and J. R. Prance, Quantum oscillations of the critical current and high-field superconducting proximity in ballistic graphene, Nat. Phys. **12**, 318 (2016).

[39] F. Amet, C. T. Ke, I. V. Borzenets, J. Wang, K. Watanabe, T. Taniguchi, R. S. Deacon, M. Yamamoto, Y. Bomze, S. Tarucha, and G. Finkelstein, Supercurrent in the quantum Hall regime, Science **352**, 966 (2016).

[40] I. V. Borzenets, F. Amet, C. T. Ke, A. W. Draelos, M. T. Wei, A. Seredinski, K. Watanabe, T. Taniguchi, Y. Bomze, M. Yamamoto, S. Tarucha, and G. Finkelstein, Ballistic Graphene Josephson Junctions from the Short to the Long Junction Regimes, Phys. Rev. Lett. **117**, 237002 (2016).

[41] M. J. Zhu, A. V. Kretinin, M. D. Thompson, D. A. Bandurin, S. Hu, G. L. Yu, J. Birkbeck, A. Mishchenko, I. J. Vera-Marun, K. Watanabe, T. Taniguchi, M. Polini, J. R. Prance, K. S. Novoselov, A. K. Geim, and M. Ben Shalom, Edge currents shunt the insulating bulk in gapped graphene, Nat. Commun. **8**, 14552 (2017).

[42] M. T. Allen, O. Shtanko, I. C. Fulga, J. I.-J. Wang, D. Nurgaliev, K. Watanabe, T. Taniguchi, A. R. Akhmerov, P. Jarillo-Herrero, L. S. Levitov, and A. Yacoby, Observation of electron coherence and Fabry-Perot standing waves at a graphene edge, Nano Lett. **17**, 7380 (2017).

[43] G. Nanda, J. L. Aguilera-Servin, P. Rakyta, A. Kormányos, R. Kleiner, D. Koelle, K. Watanabe, T. Taniguchi, L. M. K. Vandersypen, and S. Goswami, Current-phase relation of ballistic graphene Josephson junctions, Nano Lett. **17**, 3396 (2017).

[44] M. Zhu, M. Ben Shalom, A. Mishchsenko, V. Fal'ko, K. Novoselov, and A. Geim, Supercurrent and multiple Andreev reflections in micrometer-long ballistic graphene Josephson junctions, Nanoscale **10**, 3020 (2018).

[45] J. Park, J. H. Lee, G.-H. Lee, Y. Takane, K.-I. Imura, T. Taniguchi, K. Watanabe, and H.-J. Lee, Short Ballistic Josephson Coupling in Planar Graphene Junctions with In-homogeneous Carrier Doping, Phys. Rev. Lett. **120**, 077701 (2018).

[46] R. Kraft, J. Mohrmann, R. Du, P. B. Selvasundaram, M. Irfan, U. N. Kanilmaz, F. Wu, D. Beckmann, H. von Löhneysen, R. Krupke, A. Akhmerov, I. Gornyi, and R. Danneau, Tailoring supercurrent confinement in graphene bilayer weak links, Nat. Commun. **9**, 1722 (2018).

[47] F. E. Schmidt, M. D. Jenkins, K. Watanabe, T. Taniguchi, and G. A. Steele, A ballistic graphene superconducting microwave circuit, Nat. Commun. **9**, 4069 (2018).

[48] J. G. Kroll, W. Uilhoorn, K. L. van der Enden, D. de Jong, K. Watanabe, T. Taniguchi, S. Goswami, M. C. Cassidy, and L. P. Kouwenhoven, Magnetic field compatible circuit quantum electrodynamics with graphene Josephson junctions, Nat. Commun. **9**, 4615 (2018).

[49] A. W. Draelos, M.-T. Wei, A. Seredinski, H. Li, Y. Mehta, K Watanabe, T. Taniguchi, I. V. Borzenets, F. Amet, and G. Finkelstein, Supercurrent flow in multiterminal graphene josephson junctions, Nano Lett. **19**, 1039 (2019).

[50] J. I.-J. Wang, D. Rodan-Legrain, L. Bretheau, D. L. Campbell, B. Kannan, D. Kim, M. Kjaergaard, P. Krantz, G. O. Samach, F. Yan, J. L. Yoder, K. Watanabe, T. Taniguchi, T. P. Orlando, S. Gustavsson, P. Jarillo-Herrero, and W. D. Oliver, Coherent control of a hybrid superconducting circuit made with graphene-based van der Waals heterostructures, Nat. Nanotech. **14**, 120 (2019).

[51] L. Bretheau, J. I.-J. Wang, R. Pisoni, K. Watanabe, T. Taniguchi, and P. Jarillo-Herrero, Tunnelling spectroscopy of Andreev states in graphene, Nat. Phys. **13**, 756 (2017).

[52] T. Han, J. Shen, N. F. Q. Yuan, J. Lin, Z. Wu, Y. Wu, S. Xu, L. An, G. Long, Y. Wang, R. Lortz, and N. Wang, Investigation of the two-gap superconductivity in a few-layer NbSe$_2$-graphene heterojunction, Phys. Rev. B **97**, 060505(R) (2018).

[53] M. Popinciuc, V. E. Calado, X. L. Liu, A. R. Akhmerov, T. M. Klapwijk, and L. M. K. Vandersypen, Zero-bias conductance peak and Josephson effect in graphene-NbTiN junctions, Phys. Rev. B **85**, 205404 (2012).

[54] F. Pérez-Willard, J. C. Cuevas, C. Sürgers, P. Pfundstein, J. Kopu, M. Eschrig, and H. V. Löhneysen, Determining the current polarization in Al/Co nanostructured point contacts, Phys. Rev. B **69**, 140502(R) (2004).

[55] A. A. Golubov and M. Yu. Kupriyanov, Quasiparticle current of ballistic NcS'S contacts, JETP Lett. **61**, 851 (1995).

[56] G. Giovannetti, P. A. Khomyakov, G. Brocks, V. M. Karpan, J. van den Brink, and P. J. Kelly, Doping Graphene with Metal Contacts, Phys. Rev. Lett. **101**, 026803 (2008).

[57] P. A. Khomyakov, G. Giovannetti, P. C. Rusu, G. Brocks, J. van den Brink, and P. J. Kelly, First-principles study of the interaction and charge transfer between graphene and metals, Phys. Rev. B **79**, 195425 (2009).

[58] P. A. Khomyakov, A. A. Starikov, G. Brocks, and P. J. Kelly, Nonlinear screening of charges induced in graphene by metal contacts, Phys. Rev. B **82**, 115437 (2010).

[59] M. I. Katsnelson, *Graphene: Carbon in Two Dimensions* (Cambridge University Press, Cambridge, 2012).

[60] F. Miao, S. Wijeratne, Y. Zhang, U. C. Coskun, W. Bao, and C. N. Lau, Phase-coherent transport in graphene quantum billiards, Science **317**, 1530 (2007).

[61] A. V. Shytov, M. S. Rudner, and L. S. Levitov, Klein Backscattering and Fabry-Pérot Interference in Graphene Heterojunctions, Phys. Rev. Lett. **101**, 156804 (2008).

[62] A. F. Young and P. Kim, Quantum interference and Klein tunnelling in graphene heterojunctions, Nat. Phys. **5**, 222 (2009).

[63] S. Cho and M. Fuhrer, Massless and massive particle-in-a-box states in single- and bi-layer graphene, Nano Res. **4**, 385 (2011).

[64] A. L. Grushina, D.-K. Ki, and A. F. Morpurgo, A ballistic *pn* junction in suspended graphene with split bottom gates, Appl. Phys. Lett. **102**, 223102 (2013).

[65] P. Rickhaus, R. Maurand, M.-H. Liu, M. Weiss, K. Richter, and C. Schönenberger, Ballistic interferences in suspended graphene, Nat. Commun. **4**, 2342 (2013).

[66] A. Varlet, M.-H. Liu, V. Krueckl, D. Bischoff, P. Simonet, K. Watanabe, T. Taniguchi, K. Richter, K. Ensslin, and T. Ihn, Fabry-Pérot Interference in Gapped Bilayer Graphene with Broken Anti-Klein Tunneling, Phys. Rev. Lett. **113**, 116601 (2014).

[67] R. Du, M.-H. Liu, J. Mohrmann, F. Wu, R. Krupke, H. v. Löhneysen, K. Richter, and R. Danneau, Tuning Anti-Klein to Klein Tunneling in Bilayer Graphene, Phys. Rev. Lett. **121**, 127706 (2018).

[68] F. Wu, P. Queipo, A. Nasibulin, T. Tsuneta, T. H. Wang, E. Kauppinen, and P. J. Hakonen, Shot Noise with Interaction Effects in Single-Walled Carbon Nanotubes, Phys. Rev. Lett. **99**, 156803 (2007).

[69] J. Bardeen, L. N. Cooper, and J. R. Schrieffer, Theory of superconductivity, Phys. Rev. **108**, 1175 (1957).

[70] K. Maki, The behavior of superconducting thin films in the presence of magnetic fields and currents, Prog. Theor. Phys. **31**, 731 (1964).

[71] A. Kastalsky, A. W. Kleinsasser, L. H. Greene, R. Bhat, F. P. Milliken, and J. P. Harbison, Observation of Pair Currents in Superconductor-Semiconductor Contacts, Phys. Rev. Lett. **67**, 3026 (1991).

[72] B. J. van Wees, P. de Vries, P. Magnée, and T. M. Klapwijk, Excess Conductance of Superconductor-Semiconductor Interfaces due to Phase Conjugation between Electrons and Holes, Phys. Rev. Lett. **69**, 510 (1992).

[73] I. K. Marmorkos, C. W. J. Beenakker, and R. A. Jalabert, Three signatures of phase-coherent Andreev reflection, Phys. Rev. B **48**, 2811(R) (1993).

[74] M. Schechter, Y. Imry, and Y. Levinson, Reflectionless tunneling in ballistic normal-metal-superconductor junctions, Phys. Rev. B **64**, 224513 (2001).

[75] R. Meservey and P. M. Tedrow, Tunneling measurements on spin-paired superconductors with spin-orbit scattering, Phys. Rev. B **11**, 4224 (1975).